Deflectometry-Based Thermal Vacuum Testing for a Pneumatic Terahertz Antenna

Henry Quach[a], Marcos Esparza[a], Hyukmo Kang[a], Aman Chandra[a], Heejoo Choi[a,b], Joel Berkson[a], Karlene Karrfalt[a], Siddhartha Sirsi[a,c], Yuzuru Takashima[a], Art Palisoc[d], Jonathan W. Arenberg[e], Kristy Gogick Marshall[e], Christopher S. Glynn[e], Sean M. Godinez[e], Marcos Tafoya[e], Christopher Walker[a,c,#], Christian Drouet d'Aubigny[f,+], Daewook Kim[a,b,c,*]

[a]Wyant College of Optical Sciences, University of Arizona, 1630 E. University Blvd., Tucson, AZ 85721, USA
[b]Large Binocular Telescope Observatory, University of Arizona 933 N Cherry Avenue, Tucson, AZ 85721, USA
[c]Department of Astronomy and Steward Observatory, University of Arizona, 933 N. Cherry Ave., Tucson, AZ 85721, USA
[d]L'Garde, Inc., 15181 Woodlawn Avenue, Tustin, CA 92780, USA
[e]Northrop Grumman Aerospace Systems, 1 Space Park Drive, Redondo Beach, CA 90278
[f]Lunar and Planetary Laboratory, University of Arizona, 1629 E University Blvd, Tucson, AZ 85721

ABSTRACT

The Orbiting Astronomical Satellite for Investigating Stellar Systems (OASIS) is a 20-meter class proposed space terahertz observatory supported by an inflatable membrane architecture. To measure 150 mm and 1m models of the A1 reflective membrane antenna, two deflectometry configurations were designed. The smaller assembly and its corresponding deflectometer were simulated, built in our laboratory, and produce a reconstructable signal for clocked measurements of the highly-sloped pneumatic surface. We use non-sequential raytracing simulation to bound the maximum contributions of all shape errors and suggest the N-Rotations algorithm to remove the remaining radially asymmetric errors. Then, the 1m prototype assembly was tested inside a thermal vacuum chamber (TVAC). Differential deflectometry measurements tracked the 1m surface shape changes as it was subjected to a variety of environmental setpoints, cycled between three inflation gases, and also during controlled puncture. We summarize our development and results for absolute measurements as well as from TVAC testing.

Keywords: Membrane Inflatable Mirrors, Deflectometry, Large Aperture Metrology, TVAC

1. INTRODUCTION

1.1 OASIS – Science Goals and Objectives

The Orbiting Astronomical Satellite for Investigating Stellar Systems (OASIS) is a 20-meter class space observatory that will perform high spectral resolution observations at terahertz frequencies. The observatory will scout for biogenic molecules within hundreds of protoplanetary disks and will have sufficient sensitivity to explore the role water plays in the evolution of planetary systems.[1]

1.2 Geometrical Shape of Pneumatic Membranes

The immediate predecessor to this paper describes the nature of pressurized circular membranes.[2] A pressurized ideal isotropic membrane produces a spherically aberrated shape called a Hencky Curve surface.[3] If the inflated assembly is constructed from real films for space applications such as polyimide, the pressurization generates a biconic which owes its excess coma and astigmatism to the film's mechanical anisotropy.

[#]cwalker@arizona.edu, [+]cdaubign@orex.lpl.arizona.edu, [*]dkim@optics.arizona.edu

At lower inflation pressures, wrinkles sprout from perimeter of the reflector, introducing higher order spatial frequency errors.[4] These artifacts rapidly diminish at higher pressure because the stress experienced across the entire aperture grows more uniform in all directions under pneumatic loading, shown in Figure 1.
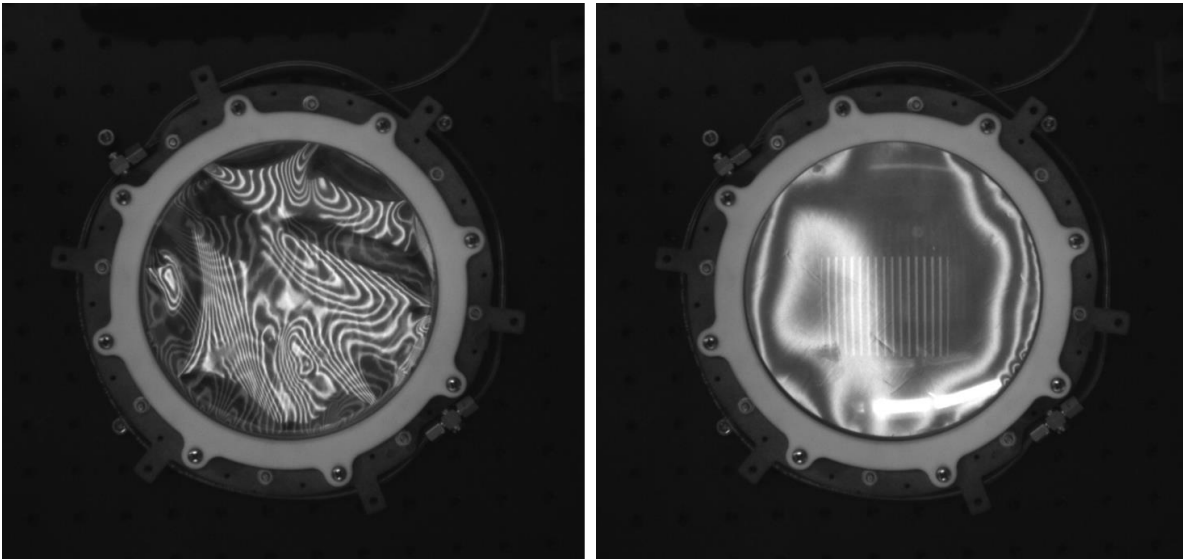

Figure 1. An inflatable 6" mylar reflector is shown on a benchtop setup. The left figure is the inflated assembly at low pressure (P = 0.007 psi), while the right achieves a turgid state at higher pressure (P = 0.016 psi). The assembly used 1 mil clear mylar for the front surface and reflective 1 mil mylar for the rear surface. The rear reflective concave surface is the optical surface of measurement. Clear 1/8" tubing mounted to the center tensioning ring release gas at two diametrically-opposed internal gas inlet holes.

The large range of possible measurable surface shape is what motivates our use of phase-measuring deflectometry. Our previous paper described how deflectometry is fast, non-contact, and can obtain full-aperture measurements of multiple inflation pressures from a single setup configuration.

The previous paper also described the difficulties in measuring inflatable UUTs (Unit Under Test) with deflectometry. One discretion is that the accuracy of geometric calibration must be commensurate with the desired accuracy of surface reconstruction. Miscalibration of one reference coordinate of the screen or camera by several microns introduces several hundred nanometers of power and astigmatism each into the final UUT surface reconstruction. This error exceeds the error budget of visible wavelength optics, but for terahertz optics, the error lies well below $\lambda/8$ rms for typical calibration uncertainties and will be demonstrated for 9 DOFS (degrees of freedom) of perturbation via a deflectometry measurement and reconstruction simulation.

1.3 Thermal Vacuum Chamber Testing

TVAC testing is a regular milestone in space flight hardware development. Emulation of the conditions of space is important to predict the behavior of hardware already demonstrated on land. Since 2019, tests of the 1m OASIS prototype at RTP (room temperature and pressure) have demonstrated focal length control as a function of internal pressure. Shape behavior is highly linear. Power increases and astigmatism decreases with incremental inflation.[2]

The next phase of characterizing the novel inflatable antenna was marked as assessed shape behavior under low temperature and pressure. A 1m OASIS prototype was measured through a clear 10" aperture acrylic TVAC chamber window. A custom deflectometer was aligned to this window, obtaining a surface reconstruction signal for the majority of the 1m aperture. The full optomechanical mounting scheme for the 1m mirror is described in detail in our sister paper.[5]

1.4 Metrology Advances and Experiments for Membrane Antennae

Our presented analyses and simulations demonstrate the suitability of deflectometry as applied to terahertz inflatable membrane reflector characterization. Our 150 mm-scale model was examined for sensitivity to calibration error using a

custom deflectometry simulator written in Zemax OpticStudio Non-Sequential and Matlab. An experimental configuration for absolute metrology with deflectometry using the N-Rotations technique acquired reconstructable signal over eight clocked positions. Finally, some key measurements for the 1m-scale OASIS primary antenna prototype in TVAC are provided. Shape measurements, taken in July 2021, tracked the dynamic slope evolution for a central clear aperture area.

2. THEORY AND SIMULATION FOR DEFLECTOMETRY SHAPE MEASUREMENT

2.1 Differential Deflectometry Theory

Historically, the challenge to global accuracy in deflectometry measurements has been accurate geometric calibration.[6] Calibration consists of finding and fitting the camera, test surface, and spatial light source, $\vec{r_c}, \vec{r_m}$, and $\vec{r_s}$, into an accurate digital representation of the physical test environment. One instructive representation of a deflectometry slope calculation, valid for slow optics, is derived from Ritter's expression for surface slopes, S_y, in the single directional case in y (a similar calculation follows in the x-slopes, S_x). [7]

$$S_y \approx \frac{1}{2}\left(\frac{y_m - y_s}{z_{ms}} + \frac{y_m - y_c}{z_{mc}}\right)$$

Here, the direction z is parallel to the optical axis of a spherical optic, the direction y in the meridional plane, and the direction x in the sagittal. If slope at each sampled point across the optic is calculated in this way, it can be observed that a mismeasurement of the lateral coordinates $\overrightarrow{y_c}$ or of $\overrightarrow{y_s}$ produces slope deviation in the final slope calculation for S_y but not S_x. Surface reconstruction with this imprecise calibration parameter is akin to miscalculating more power in the meridional plane but not additional power in the sagittal; hence, excess asymmetric shape is embedded into the deflectometry measurement across the full aperture. Similarly, a miscalibration of longitudinal coordinates $\overrightarrow{z_c}$ or $\overrightarrow{z_s}$ produces equal slope deviation in both x and y directions and produces deviation from the surface's true power.

Deflectometry's susceptibility to calibration errors in absolute measurements is well known in the metrology community, but equally known is that the subtraction of two deflectometry measurements that use identical calibration parameters produces a high-fidelity shape difference measurement.[8] If one's objective is to compare the shape of an inflatable UUT when internal pressure, external environmental temperature and pressure, or even internal gas composition are altered, *differential deflectometry* is well-poised to measure the induced shape difference. The sensitivity and accuracy of the differential variant allowed our team to precisely observe shape changes for several static environmental setpoints and even after controlled puncture in TVAC.

2.2 Shape Uncertainty due to Calibration Tolerances

We also explored methods to constrain shape error in absolute measurements arising from geometric calibration error. While interferometry requires a physical null to be manufactured to within a wave of the test optic's true shape, deflectometry requires a virtual null, or a low-order model of the ideal design surface. The assumption of an ideal model for surface calculation is not redundant with the result of an actual deflectometry test; deflectometry measurement leverages the law of reflection to determine the path of each ray from the illumination source, deflected by the UUT, and into the camera. When accurate calibration parameters are fed into the processing algorithm, accurate slopes sampled across the UUT aperture are obtained. In the integrated surface height maps, the mid-spatial and high-spatial frequencies of the UUT's true shape are revealed, which were not modeled in the virtual null.[9]

In a stricter case where we assume that the low-order surface model (i.e. RoC, radius of curvature) is not precisely known, we can estimate the bounds of surface error induced by the assumed model. To do this, we created a deflectometry measurement data acquisition simulator. Between a pinhole camera, a biconic UUT, and LCD screen in Zemax OpticStudio Non-Sequential, the behavior of deflected rays between deflectometer hardware components was simulated following the laws of geometrical optics. In Matlab, the coordinates for ~4 million ray paths and 12 million ray-surface intercepts are extracted and down-sampled to a uniformly spaced 999 x 999 pixel grid. This process obtains information as if a physical deflectometry measurement had been performed, used calibration data (perfect or erroneous) specified by a user, and was handled with our regular deflectometry processing pipeline. In Figure 2, perfect calibration parameters set was fed into the processing algorithm, and the resultant sag map was decomposed into the Noll Zernike polynomial set.[10]
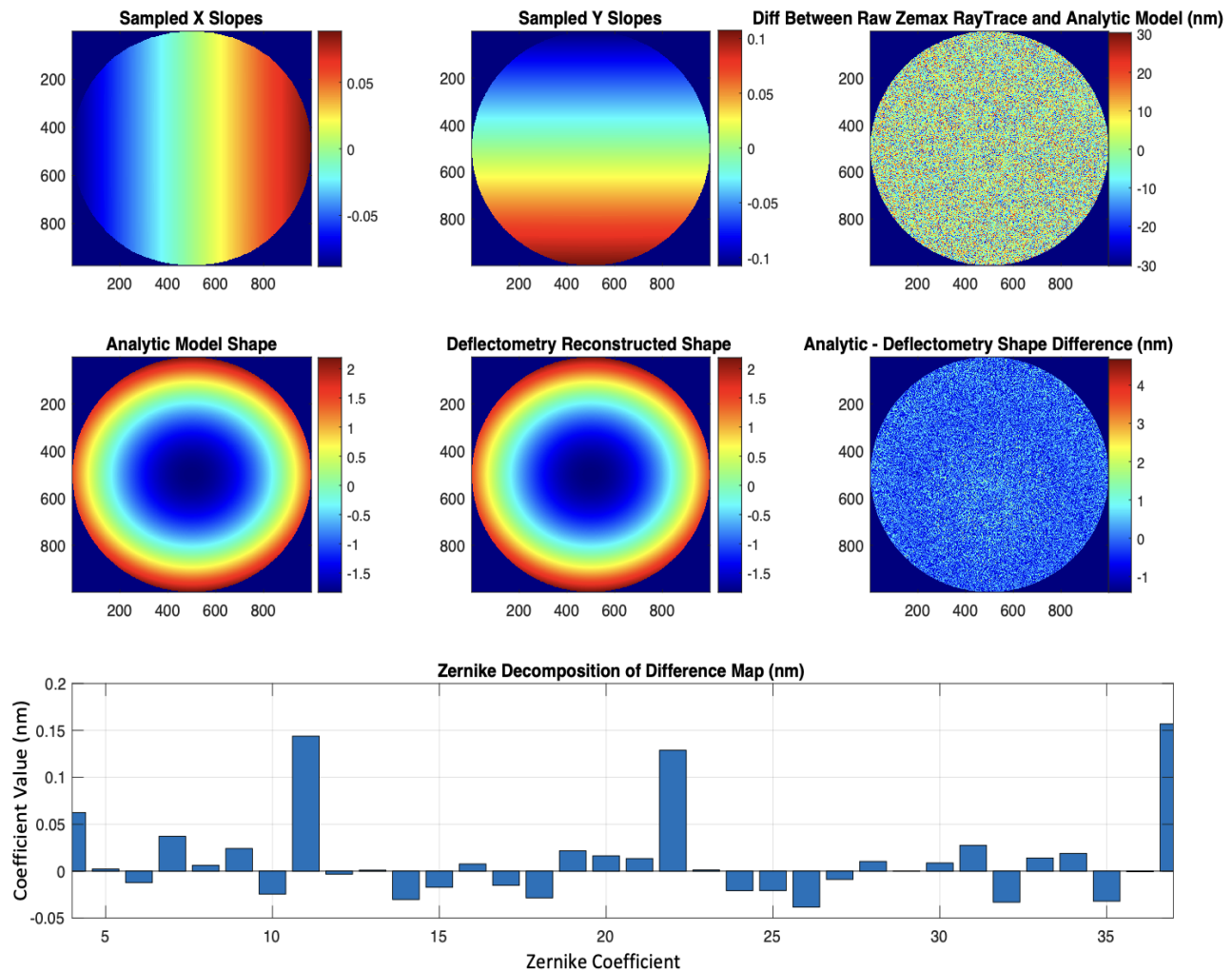
Figure 2. The reconstruction difference map shows accuracy for our reconstruction of a D = 150 mm, R_x = 850 mm, R_y = 750 mm biconic. The first two subplots plot the sampled slopes from a deflectometry acquisition with perfect phase unwrapping and ideal calibration coordinates. The virtual null's coordinates were sampled from the Zemax ray trace and cubic interpolated to a 999 x 999 grid. This grid was subtracted from the analytical expression for the prescribed aspheric biconic surface, seen on the bottom left. The interpolated ray trace surface and perfect analytical model had up to a 60 nm peak-to-valley difference due to the number of rays sampled and interpolated to the grid, shown on the upper right. Yet the errors are randomly distributed, and after a deflectometry reconstruction, the difference between the reconstruction and true analytical shape are muted, shown on the lower left.

Measurement simulations with the perfect calibration parameters showed < 1 nm RMS reconstruction accuracy for both a f/2.8 sphere (D = 150 mm) and a biconic optic (RoC_x = 850 mm, RoC_y = 700 mm). The simulator has the flexibility to use UUTs with arbitrary biconic radii and arbitrary Zernike polynomial shape terms up to Z37. With confidence that the simulator could accurately simulate the effects of miscalibration, we used the new tool to show the influence of erroneous calibration on global surface reconstruction, one calibration parameter at a time.

When nine translational rigid body degrees of freedom are perturbed by 10 mm in either direction, only primary astigmatism and power are noticeably induced. No resultant erroneous shapes beyond Z12 had a magnitude higher than tens of nanometers, as shown in Figure 3.
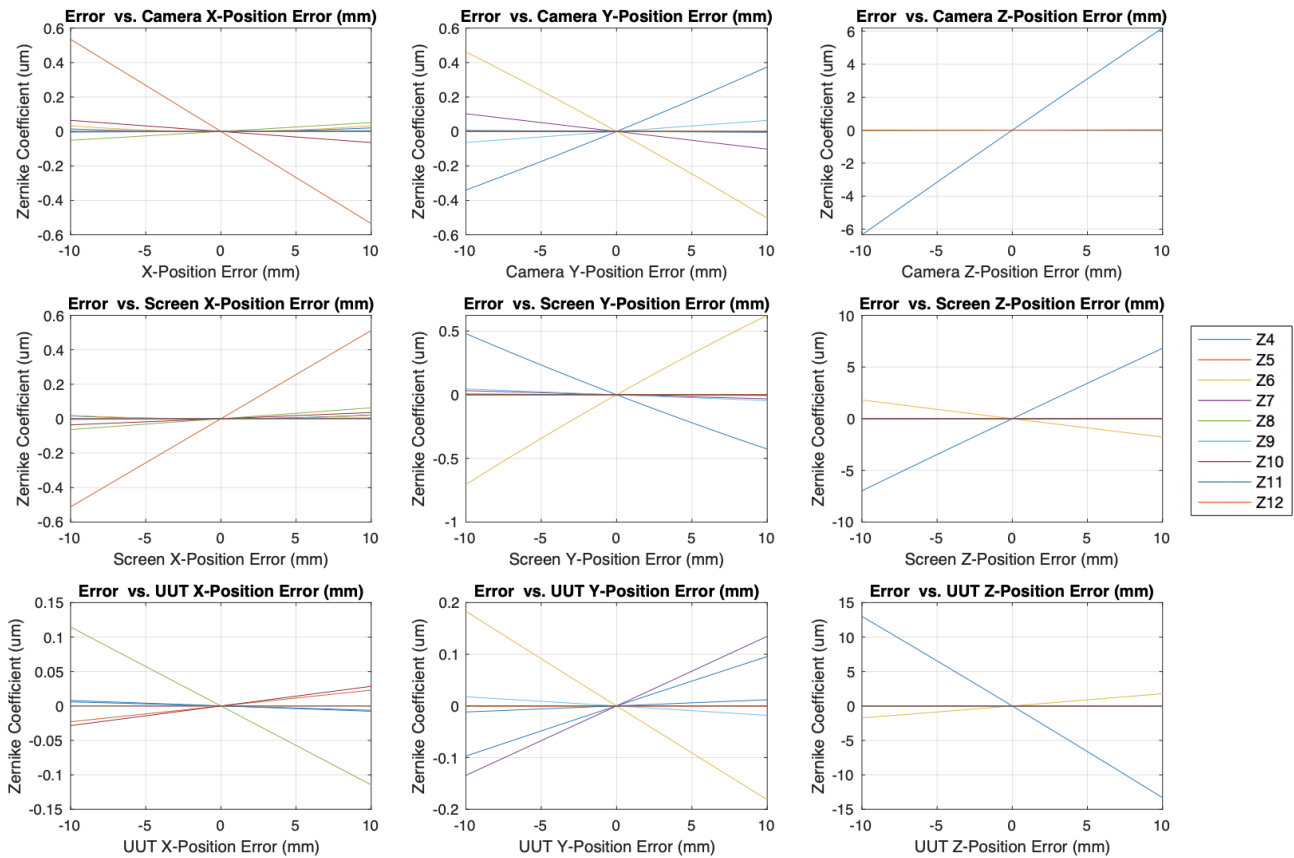
Figure 3. Perturbing the perfect calibration of the biconic UUT, surface reconstruction errors are mostly power and astigmatism. This was expected due to the reasons mentioned in 2.1. All lateral perturbations (in x and y) generate less than 0.5 μm of error for a generous 10 mm perturbation in either direction. In the longitudinal direction power was increased by up to 13 μm when the UUT z-position was imprecisely calibrated. This implies a 10 mm uncertainty with measuring the camera entrance pupil location which is rather significant. Calibration with a coordinate measurement machine is regularly accurate to within tens of microns. Longer distance laser trackers have errors that increase linearly with substantial distance; however, only several hundred microns of inaccuracy are accrued over the scale of meters.

Next, we inserted an erroneous spherical shape to act as the virtual null surface for calculation during processing. Modeling the biconic as a sphere of some varying RoC throughout the study, our deflectometry process simulation produced no erroneous Zernike polynomial coefficients higher than 12; above Z6, no coefficient appeared above 10 nanometers. However, high astigmatism (Z6) was observed, shown in Figure 4. A 150 um Z6 coefficient blows past the desired error budget and remains insensitive to the choice of spherical RoC due to the true optic being astigmatic.

To address the low order shape issue, we can use a simple experimental 4f conjugate imaging test to determine the membrane reflector's possible range of focal lengths. A small source illuminates the inflated membrane close to the UUT's mechanical axis, and is then moved backwards in the z-direction until the image of that source is coplanar with the source origin. Now that the sagittal and tangential foci are estimated, and we can use these distances as RoC_x and RoC_y to feed into the calibration parameters as the low-order shape. The uncertainty range of the visually ascertained RoCs were easily within ± 10 mm. Using estimated biconic radii of curvature on the magnitude of 10 mm for the previous test case, we produced the following surface reconstruction errors (Figure 5) when both estimated RoCs had errors of the same sign and magnitude.
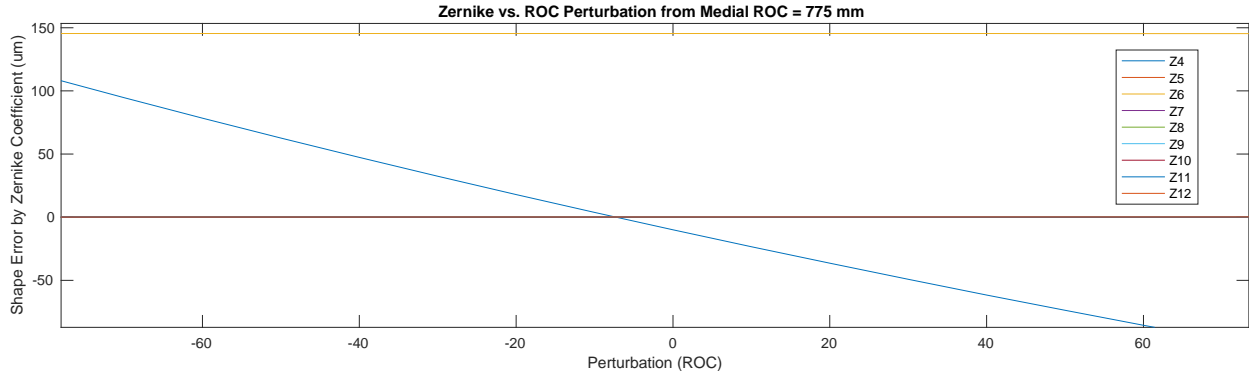
Figure 4. Because a spherical virtual null was assumed, any amount of perturbation from the 775 mm spherical RoC inherently has power error. The error is minimized when the model RoC is decreased by ~7 mm, but the Z6 astigmatism remains. All other low order shapes were effectively unimpacted by the incorrect virtual null. If the biconic was rotated by 90 degrees, Z5 would have manifested as the static shape error.
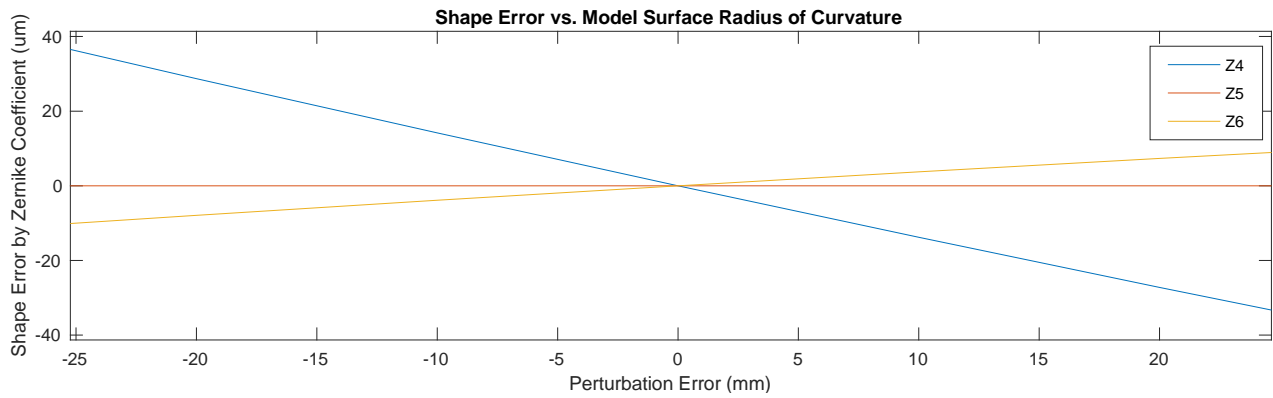

Figure 5. Unlike in the assumption of a spherical null in Figure 4, inherent assumption of a biconic with different locations of line foci produces substantially less astigmatism error even up to 25 mm perturbation, though sensitivity to the medial RoC is unchanged.

2.3 Absolute Metrology Theory

In interferometric measurements, measurement error in the surface height arises from height errors in the null reference optic. This height error can be represented as a sum of Zernike polynomials, divided into two categories - rotationally symmetric terms ($k = 0$) and rotationally asymmetric terms ($k \neq 0$).

$$W_{\text{error},arb}(r,\theta) = \sum_{i=1}^{M} Z_i = \sum_{i=1}^{M_a} Z_{i,\ rot\ symm} + \sum_{i=1}^{M_b} Z_{i,rot\ asymm}$$

When a UUT is clocked during measurement, neither the symmetric nor asymmetric null errors rotate with the clocking of the optic; only the true surface shape of the test optic rotates. This difference is manifested in a slightly different interferogram from the previous clocking position due to the static null and rotated UUT. In absolute interferometry literature, the *N-Rotations* technique takes advantage of the induced difference by making *N* equally spaced measurements at clocked positions $\theta = 360/N$.[11] After *N* measurements are made, the obtained height maps are digitally unrotated to the common position $\theta_0 = 0$, and an average is taken of all the maps. When they are digitally unrotated and averaged over N rotations, $W_{avg,error}(k) = (1/N) \sum a_l^k \cos(k\theta) + a_l^{-k} \sin(k\theta) = 0$ for all k < N, excluding k = 0.[12] For example, for N = 6, six measurements taken 60 degrees apart, digitally unrotated, and averaged, removes all asymmetric error up to Z37. The highest harmonic order represented up to that Z37 is $k = 5$.

$$W_{avg,N \, measurements} = \frac{1}{N} \sum_{1}^{N} R_{-\theta}(W_{meas})$$

$$= \frac{1}{N} \sum_{1}^{N} R_{-\theta}\big(W_{meas} + W_{error \, asym} + R_{\theta}(W_{true})\big)$$

$$= R_{-\theta}(W_{error, \, rot \, sym}) + R_{-\theta}(R_{\theta}(W_{true}))$$

$$= W_{error, \, rot \, sym} + W_{true}$$

The k-symmetry of the azimuthal terms allows all of the rotationally asymmetric error up to Z37 to simply cancel out. Unfortunately, rotationally symmetric error terms are immune to this technique. The practical use case for N-Rotations in interferometry is usually when the desired accuracy of measurement is on par with the accuracy of the manufactured null. Surface error across the aperture optic still must be within a fraction of a wavelength of the null optic for all clocked UUT positions, or else no processable interferogram signal will be present at sub-aperture UUT locations that exceed that height difference. For deflectometry, this height difference limitation for clocked positions is less inhibiting since a broad range of UUT positions can still capture a full reconstruction signal.[13] A simulation of the N-Rotations test using an erroneous spherical surface model shows the recovery of the previous biconic shape down less than 200 nm RMS.

In the case that near-perfect calibration of an optic is not assumed, we can use the N-Rotations technique to remove remaining systematic error. In Figure 6, an extreme UUT with 850 microns of Z4, and 50 microns of Z5 and Z6, and 3 microns of every single Zernike up to 37 was used in the virtual simulator for 8 rotated measurements. Calibration of all lateral parameters up was offset by +20 mm. The digital unrotation process reduced microns of the holistic induced calibration error down to less than 100 nm.
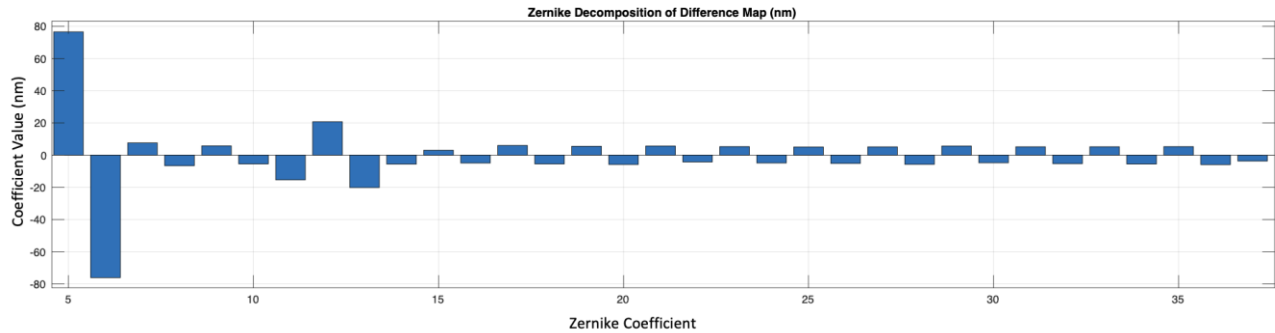

Figure 6. The Zernike decomposition of the digitally unrotated and averaged measurements depicts a substantial reduction of shape error, whose sensitivity to calibration perturbations was predicted in Figure 3. Furthermore, the null used in this case was a sphere, rather than the biconic model. Note that up to 4 μm of residual Z4 remained present after the N-Rotation test.

3. DEFLECTOMETRY-BASED METROLOGY SYSTEMS

3.1 Small-Scale Membrane Assembly Design, Manufacturing, and Preparation

We constructed a 150 mm antenna membrane assembly using clear and reflective mylar (both 1 mil thick), and clamped them between three Nylon-12 flanges. An 'undulated' double O-Ring design was present on each side to improve sealing performance, and double the number of flange bolts from previous prototypes to better help seal this assembly. The assembly was inflated until its medial radius of curvature was 800 mm. Then, the membrane was mounted atop a large Klinger motorized stepper stage, whose clocking resolution was 1.2 arcminutes.

A 12.9" iPad Pro (#A1670) and PointGrey camera (FL3-U3-13Y3M-C) were used to measure the optic. The deflectometry configuration was set for 8 different clocking positions, because fewer digital interpolation artifacts are induced when digitally rotating obtained surface maps at multiples of 45 degrees. The full configuration is shown in Figure 7 and will be tested in the near future.
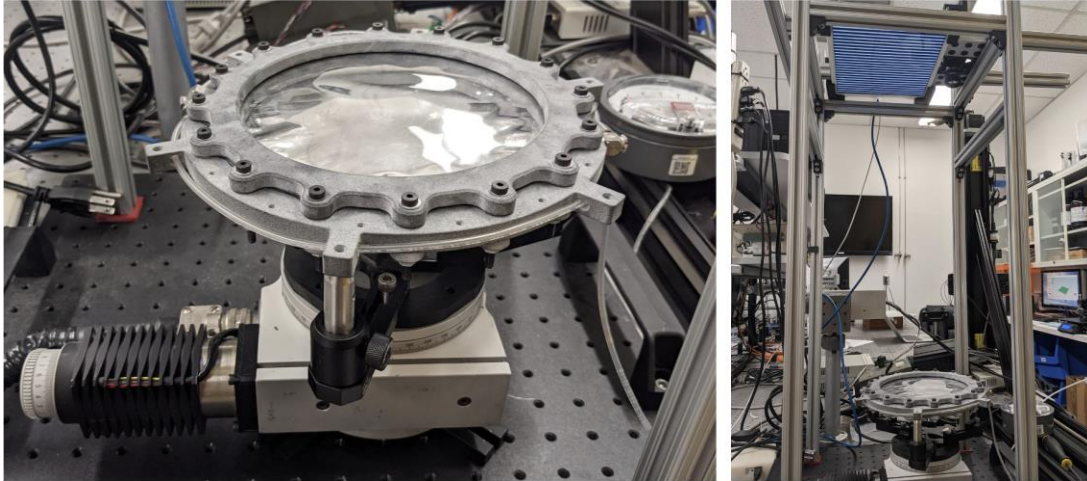
Figure 7. This is the setup for 150 mm UUT. The configuration centers the rotation stage mechanical axis to that of the UUT within 1 pixel. The camera focused at the rear concave mylar surface, and a Makita air compressor let air into the assembly. Over 8 rotations, signal was seen for 80% of the aperture diameter. Because wrinkles are highly sloped, some clocked positions showed reconstructable signal near the aperture edge, but not other clocking positions.

3.2 TVAC Test for OASIS

For TVAC testing, the 1 m UUT was oriented with its mechanical axis parallel to the inside the TVAC chamber's cylindrical axis. This UUT is identical to that of the previous tested 1 m prototype, but both mylar sheets were replaced with fresh 3-mils thick material. Behind the inflated UUT assembly, a fixed mechanical datum consisting of three spherical tooling balls was used for physical reference in proximity to the UUT vertex. Outside the chamber, a custom vacuum ready inflation control unit provided by FreeFall Aerospace maintained the internal UUT pressure to a resolution of 10 Pa. The internal pressure was nominally set to 520 Pa (0.075 Psi) relative to the chamber-controlled environmental pressure, which ranged from atmospheric (101325 Pa) to near-vacuum (0.11 Pa).

A deflectometer, shown in Figure 8, was mounted to TVAC window and aligned after the UUT was situated within the chamber for testing. This instrument consisted of a 12.9" iPad Pro (#A2378) illumination source, a Point Grey monochrome camera (FL3-U3-13Y3M-C) with a f = 12 mm lens, and machined aluminum baseplates for mounting. The camera and screen were oriented parallel to the 10" diameter TVAC window. During testing, the first Fresnel reflection at the acrylic window interface was faint enough to not significantly reduce signal contrast at the deflectometry camera detector. The entire setup is depicted in Figure 9.

Figure 8. The deflectometer frame consists of two 14" x 14" aluminum plates with mounting holes to constrain a camera and illumination screen (left). Standoffs fastened through aluminum slots allow for translation, if required. The plates were fastened to multiple 3/8" bolts standing out from the TVAC clear aperture window. The entire deflectometer assembly is rotated 22 degrees from the normal vector defined at the floor in order to match the orientation of the bolt hole pattern (right).
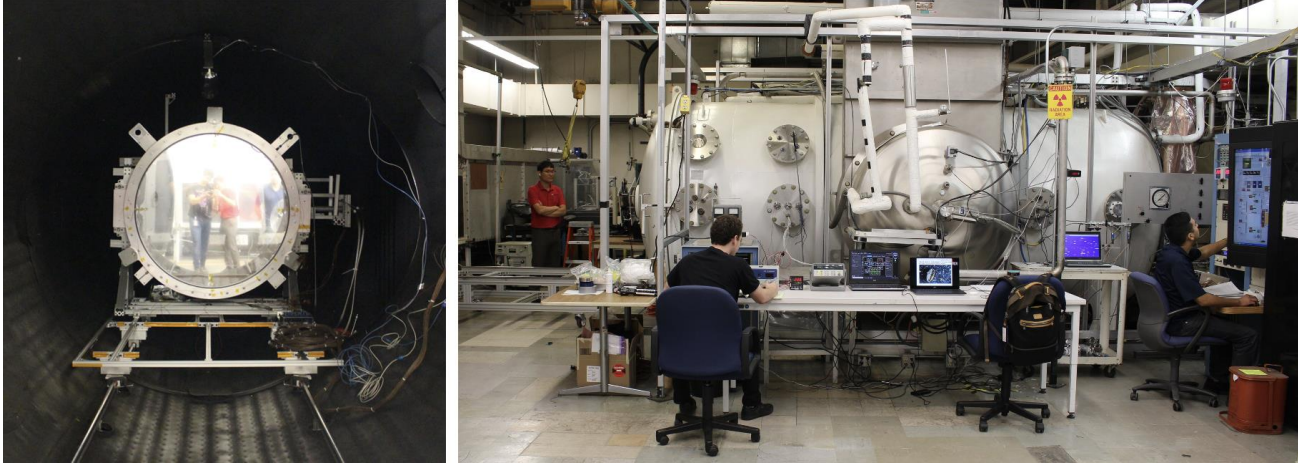
Figure 9. The 1m test article is mounted at back of the chamber cylinder, nominally 6 feet in diameter. The scale of the entire test configuration was 3.8 meters from the UUT frame to the deflectometer. A Leica laser tracker also took absolute coordinate reference measurements for future global deflectometry surface reconstruction.

4. EXPERIMENTAL TVAC RESULTS

4.1 Repeatability Measurement Within Chamber

Testing took place over the span of one week in early July at the Northrop Grumman Space Systems facility in Redondo Beach. A total of 80 surface measurements were taken of the same surface, subject to a variety of environmental setpoints within TVAC. At each fresh inflation of the membrane, the membrane vertex was brought into contact with the rear mechanical datum and then the external pressure control unit stepped back inflation pressure by 10 Pa until the surface no longer contacted the mechanical datum. When tested between successive runs, the peak-to-valley surface difference between three measurements spaced one minute apart, was only up to 4 microns. Differences in surface measurement results manifested mostly at the edge of the aperture, where wrinkles form. For an Argon gas fill, an internal pressure of 700 Pa, TVAC chamber pressure of 0.11 Pa, and chamber temperature of 137K, the total RMS difference across the surface was about 200 nanometers, shown in Figure 10.
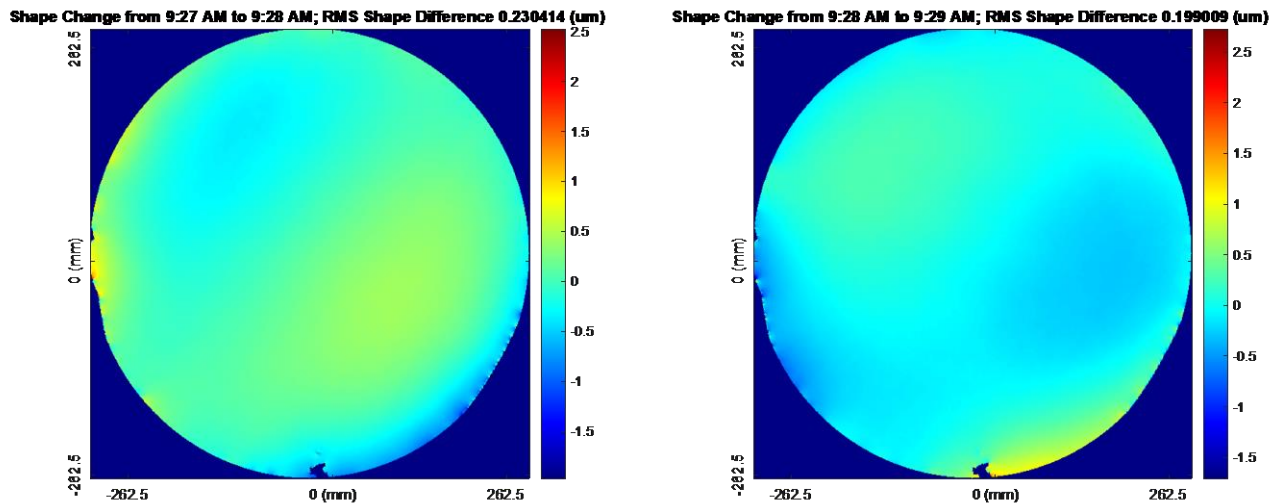

Figure 10. Two differential deflectometry measurements show the repeatability of the inner aperture. Changes were most pronounced at the edges of the aperture. At the six O' Clock position of the surface map, the article visible at 6 O'Clock is where an opaque T-type thermocouple sensor was placed. This was positioned at the front 6 O' Clock position of the frontal transparent mylar. What we see is its shadow from mechanical vignetting. All surface maps from this point forward are cropped to a common clear aperture region for visualization and surface comparison.

4.2 Internal Fill Gas Cycling

Our protocol then cycled the fill gas. Gases were injected into the membrane assembly through a port in the central tensioning ring, and later evacuated through a diametrically opposed outlet port. Helium was injected into the membrane first, followed by Argon, and then Xenon. Deflation and re-inflation with each gas were planned to be repeated several times to improve gas concentration but in practice, very slow fill and vacuum speed through the small, long gauge feed tube limited our ability to repeat the vacuum/fill cycle. As a result, the fill gas in the inflatable was never pure.

The differential measurements between surface maps of each membrane inflated by a different gas are plotted in Figure 11. Deflectometry measurements captured small changes in shape for the same ROI within several microns PV at each gas interchange, each ~30 minutes apart.
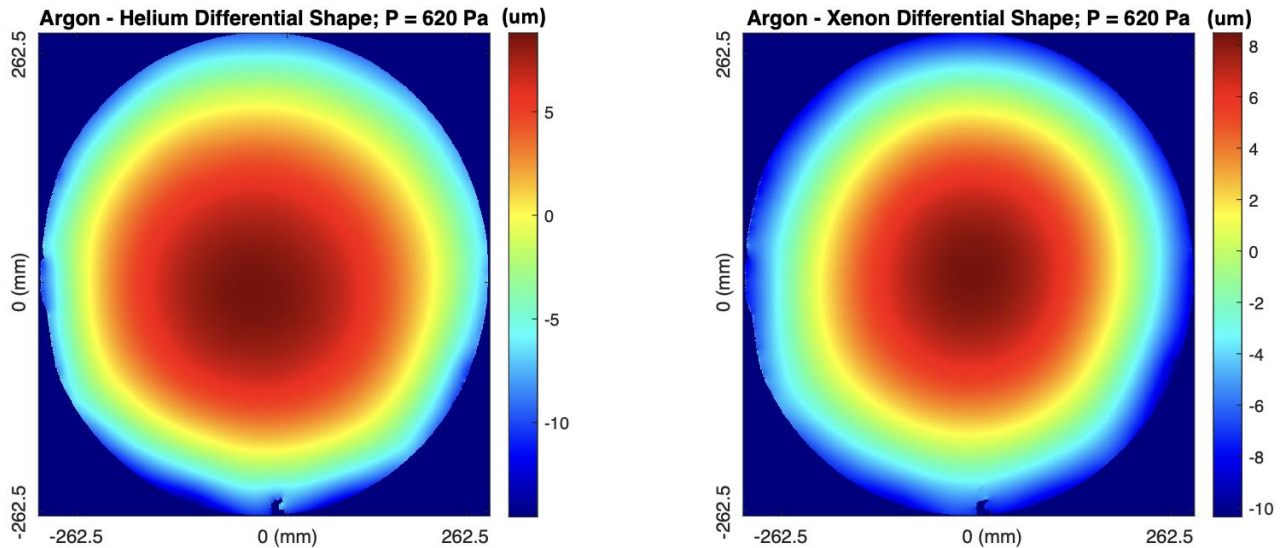

Figure 11. The differential surface maps show a power difference between the argon and helium trials, and the difference between argon and xenon trials. A power difference clearly manifests between two gases inflated to contact the mechanical datum. The surface difference is a function of inflation control stability and resolution, mechanical datum contact repeatability, and buoyancy due to differences in molecular weight.

4.3 Induced Thermal Gradient by Overhead Radiation Source

During part of the TVAC test, an overhead heat source (or 'Artificial Sun') illuminated the membrane assembly. The source was positioned closest to the aperture's 12 O' Clock position (north). Chamber temperature was set to T = 142K and pressure was at 0.11 Pa was enforced. Starting at 10:04 AM, the radiation source was activated and the reflective mylar surface began warming. Four T-type thermocouples were attached at the four cardinal points near the periphery of the front and back membranes. For the rear reflective surface, the north T-type thermocouple for the gained thermal energy the most rapidly because it was closest to the radiation source. The southern thermocouple measured the next highest average temperature, while the eastern and western thermocouples were in between.

The distribution of temperatures between the four thermocouples after a long period of time is a function of chamber geometry and radiative transfer properties. For example, the cylindrical TVAC geometry has an elevated, sliding rectangular base for mounting. This feature, rising from the floor of the chamber, breaks azimuthal geometry and allows different equilibrium temperatures to be reached between the top and bottom of the 1m UUT assembly. In Figure 12, the temperatures of all four rear thermocouples are plotted.

Throughout the test, temperature was T = 142K and chamber pressure was P = 0.11 Pa. In the final half hour, the temperature of the north thermocouple indicated a change of 2K. In Figure 13 each differential map shows the change in shape from the initial surface captured from 10:44 AM, showing the difference in shape from each preceding map. The evolution of the thermal gradient can be visually ascertained but also calculated. The RMS difference from the first two subplots grew to ~2 μm by subplot 8. By 11:00 AM, the thermal expansion of the mylar was sufficient to bring the concave surface in contact with the mechanical datums.
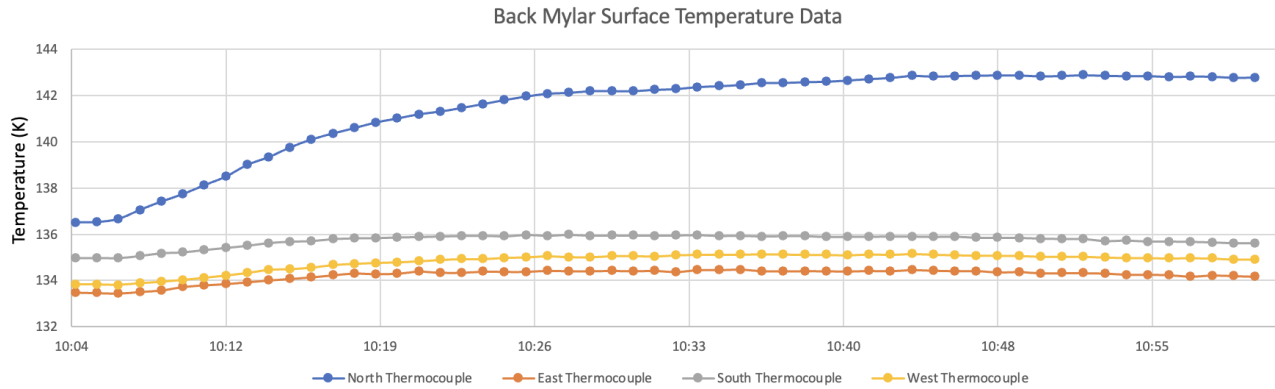
Figure 12. Starting at 10:04 AM, the artificial sun was turned on. For the next half hour, the temperature rose by 1K for the east, west, and south thermocouples, but the rose by 5K for the north sensor.
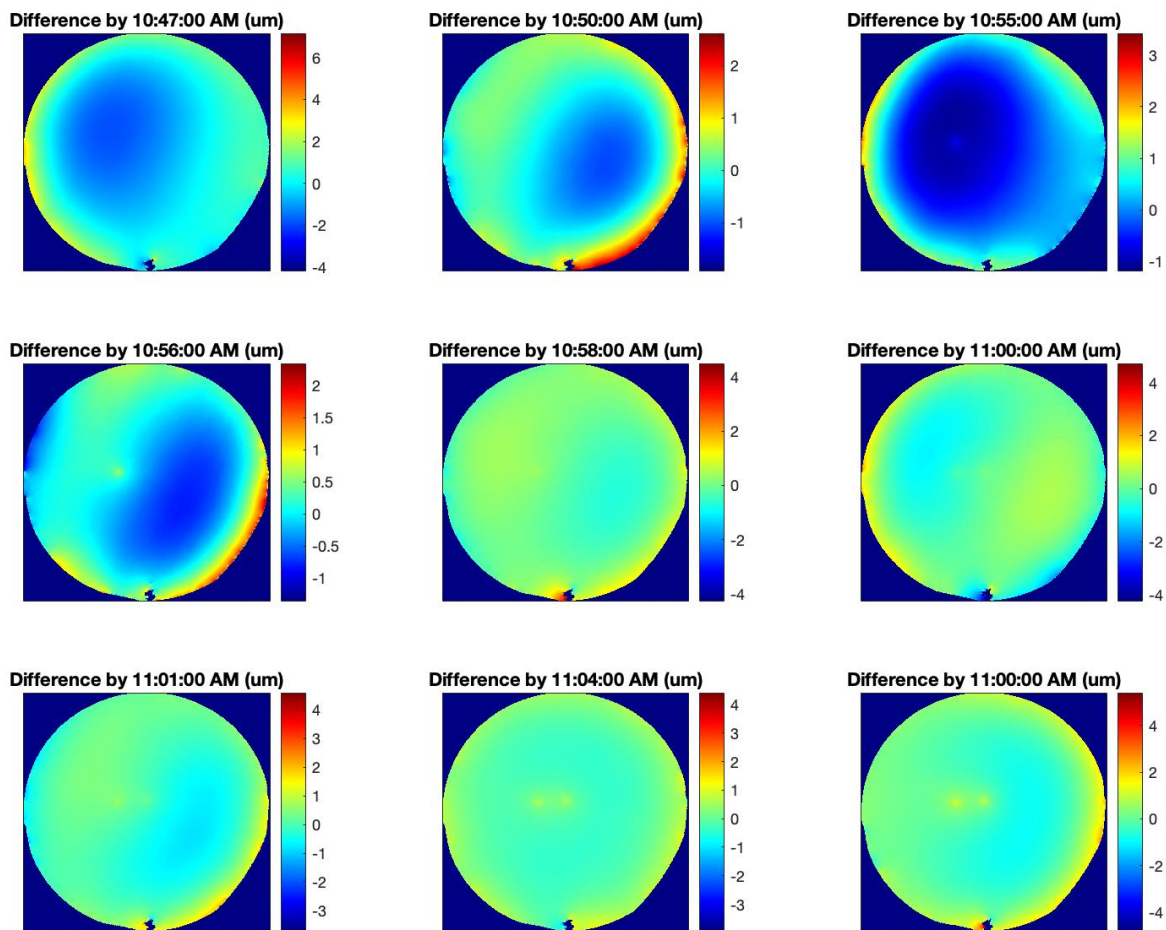

Figure 13. Shape difference are observed successively every 1-3 minutes. The rear reflective mylar absorbs energy and ever so slightly change its elastic modulus. Eventually, this change is sufficient to stretch the membrane several μm to contact the three rear mechanical tooling balls. These datums are the yellow dots near the center of subplots 8 and 9. Spatial dimensions are the same as in Figure 11, with a radius of 262.5 mm, but all maps.

4.4 Surface Puncture Test

The last segment of our test protocol was a puncture test shown in Figure 14 - 15. A feature of Northrop's TVAC chamber added for this test is an externally-controllable arm. The mechanical actuator wields a thin needle, which moves in an arc to pierce a hole into the back reflective membrane. The spatial location was chosen at the north cardinal position near the aperture edge of the membrane assembly. Figure 14 reveals the reconstruction signal with no puncture, with puncture 1 minute later, and puncture 2.5 minutes later. The shadow in the third subplot indicates that the slope is steep enough to exceed the dynamic slope measurement range of the deflectometer configuration. Interesingly, at almost 4 minutes from puncture, the assembly cyclically recovered from the initial pressure ripple such that full central aperture measurements can be made again.
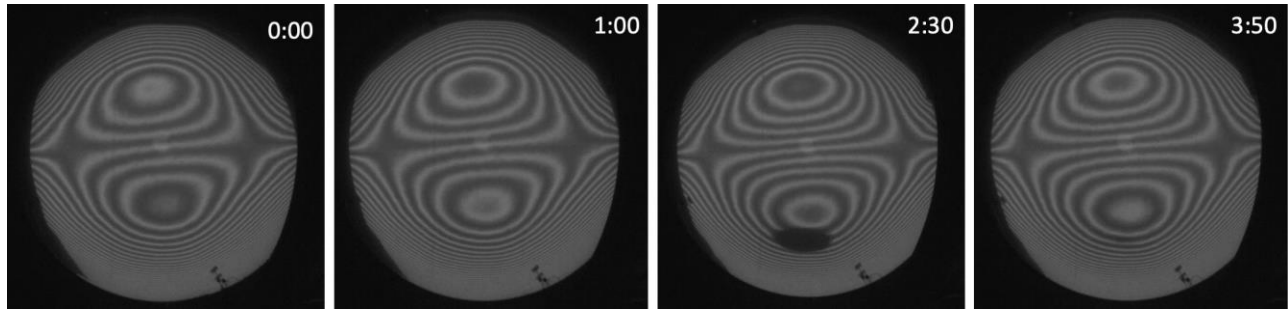

Figure 14. After the unpunctured reflector (first subplot) is punctured, the number of fringes increases (second subplot). The change indicates a shape difference, particularly power. 2.5 minutes later, a shadow precludes measurement at this local surface region (third subplot). The shadow shrinks and grows at a low temporal frequency until it fully recovers in the last image. Deflectometry measurement is capable of reconstructing most of the aperture even when no signal is present within a sub-aperture, but is more difficult to compare using commonly-used full-aperture representations.
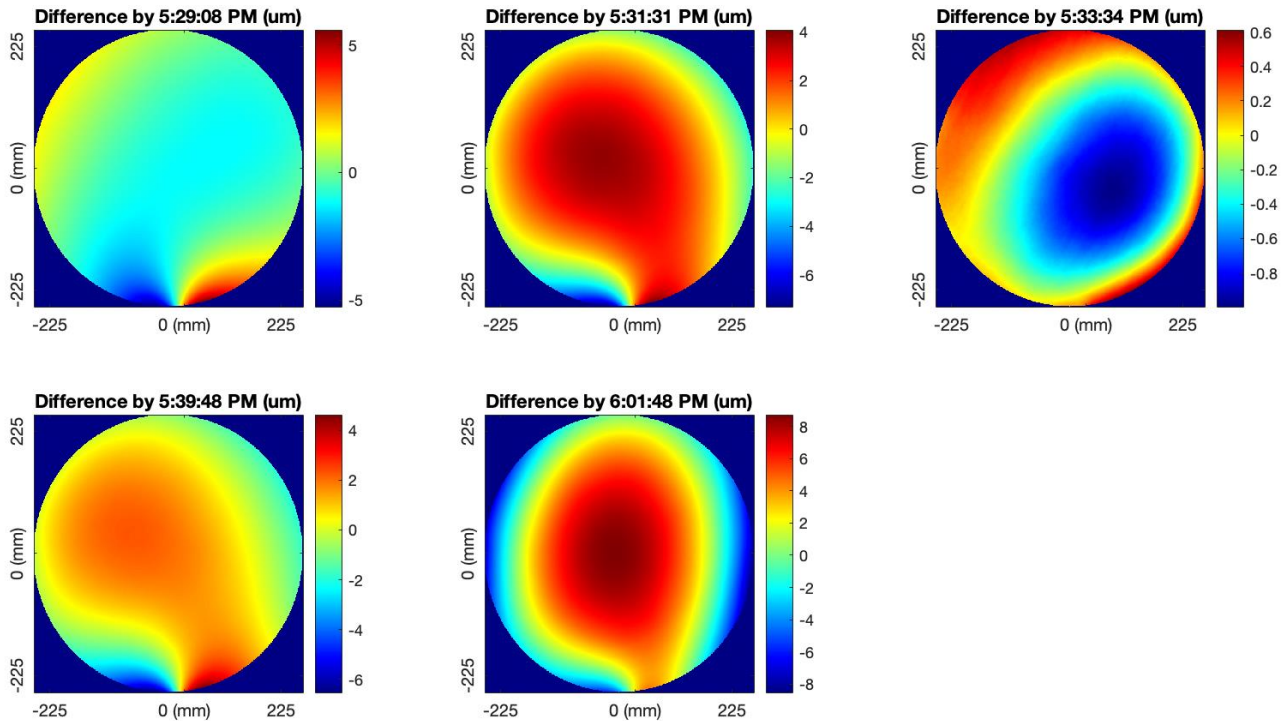

Figure 15. The cyclic undulation between 5:26:40 to 5:39:48 occurred on the scale of tens of seconds (subplots 1-4), but the magnitude of the ripple flattened by 5:45 PM. 15 minutes after the first puncture, the team made a second puncture, shown in subplot 5. The undulation ripples grew larger and up to 16 microns in magnitude.

Figure 15 shows full center aperture measurements whenever the unmeasurable shadow disappears. Interestingly, the southern thermocouple becomes a heightened node after puncture, moving closer to the deflectometer. To observe the surface effects of the main subaperture, the radius of the common analysis aperture was decreased by 40 mm. Shape changes reflect different phases of the cyclic pressure ripple – spaced two minutes apart, the first four subfigures show differences increasing up to 10 μm PV and as low as 1.5 μm PV. The plots show surface shape subtractions from the original unpunctured surface measurement taken at 5:26:40 PM.

5. SUMMARY AND CONCLUSION

We demonstrate methods to bound the influence of the calibration uncertainties that introduce surface reconstruction errors in deflectometry for pneumatic membranes. A deflectometry reconstruction simulator for arbitrary biconic and Zernike shapes showed generous amenability to calibration errors on the order of millimeters, under a tolerance budget dictated by the science wavelength on the order of tens of microns. A N-Rotations test was also simulated and its experimental setup will be tested in the future. Finally, TVAC testing was conducted at low-temperature, near-vacuum conditions for repeatability, gas cycling, induced thermal gradients, and puncture. The full extent of data has yet to be examined, but the reported results show a positive outlook for a larger-scale membrane, characterized at atmosphere and in TVAC.

ACKNOWLEDGEMENTS

REFERENCES

[1]   Walker, C., Kulesa, C., Smith, I. S., Perry, W., Kim, D., Palisoc, A., Cassapakis, C., Crowe, D. and Pierce, D., "Orbiting Astronomical Satellite for Investigating Stellar Systems (OASIS): Following Water from the Interstellar Medium to Oceans," Bull. AAS (2019).

[2]   Quach, H., Berkson, J., Sirsi, S., Choi, H., Dominguez, R., Duffy, B., Lesser, D., Takashima, Y., Palisoc, A., Walker, C. and Kim, D. W., "Full-aperture optical metrology for inflatable membrane mirrors," Opt. Manuf. Test. XIII(August), 20 (2020).

[3]   Hencky, H., "Über den Spannungszustand in kreisrunden Platten," Zeitschrift für Angew. Math. und Mech., 311–317 (1915).

[4]   Chandra, A. and Walker, C. K., "Thermally formed inflatable reflectors for space telescopes," Conf. IEEE Aerosp. Conf. AERO 2020 (2020).

[5]   Esparza, M. A., "Stressed Deformable Reflector and Pneumatic Membrane Antenna for Thermal Vacuum Terahertz Wavefront Control and Measurement," Astron. Opt. Des. Manuf. Test Sp. Gr. Syst. III, SPIE—The International Society for Optical Engineering (2021).

[6]   Huang, L., Idir, M., Zuo, C. and Asundi, A., "Review of phase measuring deflectometry," Opt. Lasers Eng. **107**(August), 247–257 (2018).

[7]   Ritter, R. and Hahn, R., "Contribution to analysis of the reflection grating method," Opt. Lasers Eng. **4**(1), 13–24 (1983).

[8]   Kam, J., "Differential Phase Measuring Deflectometry for High-Sag Freeform Optics" (2019).

[9]   Huang, R., Su, P., Horne, T., Brusa, G. and Burge, J. H., "Optical metrology of a large deformable aspherical mirror using software configurable optical test system," Opt. Eng. **53**(8), 085106 (2014).

[10]   Noll, R. J., "Zernike Polynomials and Atmospheric Turbulence.," J Opt Soc Am **66**(3), 207–211 (1976).

[11]   Evans, C. J. and Kestner, R. N., "Test optics error removal," Appl. Opt. **35**(7), 1015 (1996).

[12]   Parks, R. E., "Removal of Test Optics Errors," Adv. Opt. Metrol. I, **0153**(December 1978), 56–63 (1978).

[13]   Faber, C., Olesch, E., Krobot, R. and Häusler, G., "Deflectometry challenges interferometry: the competition gets tougher!," Interferom. XVI Tech. Anal. **8493**(September 2012), 84930R (2012).